

# Signatures of ~~midlatitude~~ Eurasian heat waves in global Rossby wave spectra

Iana Strigunova, Richard Blender, Frank Lunkeit, and Nedjeljka Žagar

Meteorological Institute, Center for Earth System Research and Sustainability (CEN), Universität of Hamburg, Grindelberg 5, 20144 Hamburg, Germany

**Correspondence:** Iana Strigunova (iana.strigunova@uni-hamburg.de)

**Abstract.** ~~The This~~ paper investigates systematic changes ~~of in~~ the global atmospheric circulation ~~during midlatitude~~ statistics during Eurasian heat waves. ~~The global balanced circulation is defined in terms of the Rossby wave solutions of the linearized primitive equations. The circulation variability is assessed by the probability density functions (PDFs) of the normalized total energy anomalies investigation of Rossby wave energy anomalies during heat waves is based on the time series of~~  
5 Hough expansion coefficients representing Rossby waves with the troposphere-barotropic structures during the extended boreal summer in the ERA5, ERA-Interim, JRA-55, and MERRA reanalyses. The climatological Rossby-wave energy distribution is shown to follow a  $\chi^2$ -distribution with skewness dependent on the zonal scale.

The heuristic approach reveals signatures of Eurasian surface heat waves on global energy spectra. It is shown that the skewness in planetary waves increases during Eurasian heat waves while the opposite occurs in the zonal mean flow. No change  
10 in the skewness is found in synoptic-scale Rossby waves. Instead, synoptic zonal wavenumbers  $k = 7 - 8$  are characterised by a statistically significant increase of about 5% in the intramonthly variance with respect to their climatological values. The evaluation is performed in wavenumber space defined by the zonal wavenumbers, meridional modes and vertical structure functions. Heat waves are defined by spatially averaged surface temperatures in Eurasia (bounded by the Ural) above the 95% percentile on at least three consecutive days. Normalized energy anomalies of the Rossby waves are found to be  $\chi^2$ -distributed  
15 with a skewness associated with the climatology. The largest increase of about 20% in the intramonthly variance is found in the number of degrees of freedom. The PDFs of energy anomalies during heat waves are compared with their climatological distributions for the zonal mean flow, for the planetary and for the synoptic scales. During zonal mean state asymmetrical Rossby wave with the meridional index 6 along with the decrease in the mode 4. This reflects the weakening of the mean westerlies near their core at  $45^\circ\text{N}$  and their strengthening at higher latitudes around  $75^\circ\text{N}$ .

20 Keywords: Eurasian heat waves, Rossby waves, global energy spectra, circulation statistics, skewness, entropy, intramonthly variance

*Copyright statement.* TEXT

# 1 Introduction

Heat waves, periods with the daily maximum temperatures exceeding the climatological conditions by certain thresholds, have been increasing in numbers and magnitude, especially over Eurasia (e.g., Rousi et al., 2022). While the current operational numerical weather and ensemble prediction systems forecast such extremes several weeks ahead (e.g., Emerton et al., 2022), understanding the mechanism and dynamics of heat waves poses a challenge. Heat waves are connected with persistent high-pressure systems (blockings). Numerous studies focus on the onset and drivers of blocking; however, no consensus exists due to complexity of dynamical and thermodynamical processes involved (e.g., Kautz et al., 2022). Blockings are often parts of large-scale quasi-stationary wave patterns (e.g., Stefanon et al., 2012). On one side, persistent weather patterns are part of internal variability. On the other side, the effect of climate change on the frequency and persistence of these patterns is still under debate (Woollings et al., 2018). For example, Park and Lee (2019) showed that these persistent weather patterns can be forced or triggered by remote anomalous tropical heating (“tropical forcing”). While the physical mechanisms leading to blockings are under discussion (Petoukhov et al., 2013; Nakamura and Huang, 2018; Teng and Branstator, 2019; Wirth and Polster, 2021), the quasi-stationary behaviour of these wave patterns is shown to lead to concurrent extreme events (Kornhuber et al., 2020; Fuentes-Franco et al., 2021).

In contrast to previous studies investigating particular aspects of heat waves, ~~the skewness of PDFs of planetary-scale circulation is increased up to a factor of two. The increase is associated with a drastic~~ our research aims to identify changes in the global Rossby-wave circulation statistics during Eurasian heat waves. While a number of studies addressed particular aspects of heat waves over Eurasia (e.g., Feudale and Shukla, 2011; Schneider et al., 2012; Trenberth and Fasullo, 2012; Drouard and Wernitz, 2021), their effects on the global spatiotemporal variance spectra have not been studied. We analyze the global three-dimensional (3D) circulation during Eurasian heat waves in terms of horizontal and vertical scales of the Rossby waves and compare it with the global circulation climatology. As we show, the probability density function (PDF) of the Rossby-wave circulation, which is described by the  $\chi^2$ -distribution, changes during Eurasian heat waves. The changes are quantified by skewness and entropy measures for different zonal wavenumbers. The associated reduction of the number of active degrees of freedom ~~down to 1/4~~ compared to climatology ~~;-This reduction explains can be used to explain~~ the coarse structure of blocking events in the midlatitude troposphere ~~as confirmed by the reconstructed circulation in physical space. The changes in variability are also assessed by investigating submonthly circulation variance across scales. Planetary waves are found to be more persistent during heat waves, while the synoptic waves vary more, which is consistent with~~.

The distributions of atmospheric fields are in general known to be non-Gaussian (Sura et al., 2005; Perron and Sura, 2013). However, ~~the idea of circulation blocking during the extreme heat events. The presented diagnostics can be applied for other extreme events in the atmosphere.~~

~~Keywords: heat waves, Rossby waves, variability changes, global energy distribution, skewness~~

Central Limit Theorem may still be applicable when the sums of components in high-dimensional systems are involved, with assumptions of independent and identical distributions of summing components<sup>1</sup>. As we demonstrate, the distributions of anomalies in atmospheric energy can appear visually close to the normal distribution due to the Central Limit Theorem. However, the energy anomaly distributions are still skewed, which can be considered as an inherited property from energy ( $\chi^2$ -distributions). The skewness,  $\gamma$ , of the  $\chi^2$ -distribution is given by  $\sqrt{8/df}$  and the excess kurtosis,  $\kappa$ , is given by  $12/df$  with the number of independent degrees of freedom denoted  $df$  (Wilks, 2011). In the  $\chi^2$ -distribution, the term “degrees of freedom” is defined by the number of sum of squares of independent (uncorrelated) normally distributed variables. In our analysis, the number of degrees of freedom is the number of all possible modes used in the projection, while the number of active degrees of freedom is a measure of the concentration of energy in large wavenumbers during a heat wave. It is important that localized structures like blocking do not consist of a finite set of low wavenumber modes but can also include contributions from higher wavenumbers (as is the case for Fourier series). Therefore, the number of active degrees of freedom is not a sharp condition but can be used to measure the system’s complexity. Note that because the atmospheric circulation is the composite of the zonal mean state and the superposition of waves which might be dependent, the statistical properties might deviate from the ideal situation.

Advanced statistical methods are common tools in the research of extreme weather events. For example, Galfi and Lucarini (2021) analyzed surface heat waves using Large Deviation Theory and found that the associated persistent atmospheric patterns are not typical (in the statistical sense) compared to the climatology but follow a dynamics which is already encoded in the natural climate variability. Lucarini and Gritsun (2020) considered blockings as manifestations of Unstable Periodic Orbits and their stability as an indicator of predictability and the involved number of degrees of freedom. They find low predictability at the onset and the decay, and increased predictability in the mature phase of blocking events in the Atlantic.

~~The enhancement of planetary and synoptic-scale Rossby waves has been linked to the occurrence or formation of heat waves in mid-latitudes. However, the relation between anomalies in global Rossby circulation and heat waves remains unclear. Moreover, there is no robust method allowing us to identify signatures of heat waves in the global atmospheric spectrum. As a possible way to determine signatures common not only for case studies of heat waves but for their composite, statistical analysis can be a suitable tool. Statistical properties of mid-latitude circulation during extreme events were examined by recent studies (Screen and Simmonds, 2014; Coumou et al., 2014; Kornhuber et al., 2019). They have identified significant~~ A more common tool for the examination of midlatitude circulation during heat waves is the Fourier series analysis of single variable data along the latitude circles. This approach identifies anomalies in the planetary- and synoptic-scale Rossby waves ~~by using during extreme events in terms of~~ the Fourier amplitudes and phases of temperature ~~and wind variables~~. Namely, ~~Screen and Simmonds (2014) have~~, geopotential or wind variables at different levels. For example, Screen and Simmonds (2014) found a significant increase in the monthly variance and mean of anomalies of the Fourier amplitudes of 500 hPa geopotential heights for zonal wavenumbers 3-8 and suggested that amplified planetary waves are connected with temperature and precipitation extremes. Coumou et al. (2014) ~~have~~ analyzed wind fields at 300 and 500 hPa and found out that zonal wavenumbers

<sup>1</sup>Under the independence of components or variables in a high-dimensional system, one can consider that its time series are uncorrelated. The identity of distributions of summing components can be regarded in terms of their mean and variances being equal.

6-8-6-8 are the most probable candidates for quasi-resonance ~~conditions~~ (amplified quasi-stationary Rossby waves due to the resonance with free waves trapped within the waveguide) according to Petoukhov et al. (2013). More recently, Kornhuber et al. (2019) ~~have shown~~ showed the coupling between the ~~wavenumber 7~~ zonal wavenumber 7 in daily wind and temperature data ~~on several vertical levels (850, 700, 500, 300) and surface extreme events~~ at several standard pressure levels and surface extremes, such as heat waves and floods which occurred during the boreal summer 2018. ~~The drawback of the one-dimensional Fourier method, performed along the latitude circles, is its lack of coupling between mass and velocity fields. We suggest the NMF decomposition as more rigorous compared to the Fourier approach because the NMF is a multivariate decomposition that represents simultaneously the velocity and mass fields using the Hough harmonics.~~

95 ~~The NMF decomposition projects three-dimensional (3D) geopotential and wind data on the Rossby and inertia-gravity waves, which are eigensolutions of~~ Our heuristic approach to spectral analysis of heat waves considers the horizontal and vertical scales simultaneously by using the normal-mode function (NMF) decomposition to project daily circulation fields onto Rossby and non-Rossby components (Kasahara, 2020). The NMF decomposition is multivariate meaning that the ~~linearized primitive equations on the sphere (Žagar N. and J., 2020).~~ We use reanalysis data decomposed using this approach to analyse  
100 ~~wind and geopotential variables are represented by the same spectral expansion coefficient thereby separating the circulation into the balanced (or Rossby) and unbalanced (non-Rossby) components~~<sup>2</sup>.

Previous applications of the NMF decomposition showed that modal analysis complements other methods of analysing global circulation by providing scale- and dynamical regime dependent information on the variability and by quantifying it in wavenumber space (Žagar et al., 2017, 2020, 2019). Žagar et al. (2020) quantified amplitudes and trends in midlatitude  
105 ~~traveling and quasi-stationary Rossby waves and in the equatorial wave activity in the reanalysis data. They found a statistically significant reduction of subseasonal variance in Rossby waves with zonal wavenumber  $k = 6$  along with an increase in variance in wavenumbers  $k = 3 \sim 5$  in the summer seasons of both hemispheres. However, they did not attempt to relate these changes with the surface weather or extreme events. This task is carried out in the present study.~~

Our goal is to investigate whether and how surface heat waves ~~in~~ during boreal summer over Eurasia affect the global  
110 atmospheric variability spectrum. ~~Therefore, we aim at answering the following question: how do heat extremes appear in the global atmospheric variability spectrum?~~ While it is not evident ~~a priori that surface heat waves during boreal summer have their fingerprints in the whole atmosphere~~ ~~a priori that regional heat waves have their signatures in the global~~ Rossby wave spectra, we show that this is, in fact, the case. ~~We carry out statistical analysis on the time series of the Hough expansion coefficients of the 3D reanalysis data similar to Žagar et al. (2020) and references therein. This statistical analysis allows us,~~  
115 ~~for the first time, to estimate the distribution of the global Rossby circulation and its total energy.~~

~~The distribution of atmospheric fields are in general shown to be non-Gaussian (Sura et al., 2005; Perron and Sura, 2013) However, the Central Limit Theorem may still be applicable when the sums of components in high-dimensional systems are involved, with assumptions of independent and identical distributions of summing components. Under the independence of component or variable in a high-dimensional system, we consider that its time series are uncorrelated. The identity of~~

---

<sup>2</sup>The real-time decomposition of the ECMWF circulation in Rossby and non-Rossby components is available on the MODES webpage <https://modes.cen.uni-hamburg.de>.

120 distributions of summing components can be regarded in terms of their mean and variances being equal. In our analysis, it is not strictly necessary that the Hough coefficients are independent and identically Gaussian distributed since we assess First, we demonstrate statistically significant changes in the energy distributions. These changes are diagnosed considering the skewness of the distributions. Even in the interpretation of the number of active degrees of freedom, we consider changes and not absolute values. Thus, the assumption of independent Gaussian distributed coefficients is not essential for interpreting the results. Nevertheless, we find that the Gaussianity of the coefficients and the corresponding  $\chi^2$ -distribution of the energy in individual modes are satisfied to a high degree.

The skewness,  $\gamma$ , of the  $\chi^2$ -distribution is given by  $\sqrt{8/df}$  and the excess kurtosis,  $\kappa$ , is given by  $12/df$  with the number of independent global total energy anomalies PDFs during heat waves. Then, we interpret the dynamics of the planetary Rossby waves through the change in active degrees of freedom,  $df$  (Wilks, 2011). Because the atmospheric circulation is the composite of the zonal mean state and the superposition of waves (or the sum of multiple modes because of orthogonality of 3D eigenfunctions) which might be dependent, the statistical properties might deviate from the ideal situation. Further, we demonstrate that the distributions of the energy anomalies can appear visually close to the Normal distribution due to the Central Limit Theorem for large degrees of freedom. However, the energy anomalies distributions are still skewed, which can be considered as an inherited property from energy distributions. For this reason, we consider skewness as the primary measure to characterise the behaviour of the Rossby circulation during the and show its relation with the entropy reduction during Eurasian heat waves.

The paper is organized as follows. The data 3D decomposition method, statistical analysis and the heat waves identification algorithm are explained in Section 2. In Section 2.2 we describe the data used for NMF decomposition and identification algorithm. In Section 3 Section 3 contains results. First, we present examples of the NMF decomposition for two recent heat waves. This is followed by the results of statistical analysis (climatology and during heat waves) and further of spatial spectra (climatological and heat waves energies) and its interpretation by filtering part of Rossby parts of balanced circulation back to physical space. In the last chapter of Section 3 Finally, we discuss how temporal variance spectra changes change during heat waves. In Section 4 we present final remarks Conclusions are presented in Section 4.

## 2 Method and Data

### 145 2.1 Normal-mode function decomposition

In this section we describe our research method that makes use of the NMF decomposition and the MODES software (Žagar et al., 2015) . The method is applied to the four modern reanalysis datasets. We present the selection method for the spectral expansion coefficients suitable for heat waves and the criteria for Eurasian surface heat waves.

Three-dimensional wind and geopotential fields are projected on NMFs in modal space. NMFs consist of

### 150 2.1 Normal-mode function decomposition of global circulation

The NMF decomposition is carried out in the terrain-following, global coordinate system  $(\lambda, \varphi, \sigma)$ , where  $\sigma$  is the ratio of the vertical level pressure and the surface pressure,  $\lambda$  denotes longitude and  $\varphi$  is latitude. At every time step  $t$ , the horizontal winds  $(u, v)$  and geopotential height  $(h)$  on  $\sigma$  levels are projected to precomputed vertical and horizontal structure functions (VSFs and HSFs, respectively). The VSFs are the numerical solutions of the vertical structure equation and HSFs are where as the HSFs are eigensolutions of the Laplace equation without forcing and are given in terms of the Hough harmonics. The projection is performed in two steps (Žagar et al., 2015). In the first step, the data  $\mathbf{X}(\lambda, \phi, \sigma)$  with longitude  $(\lambda)$ , latitude  $(\phi)$ , vertical level (Hough harmonics are defined as a product of the latitude-dependent Hough functions and harmonic waves in the longitudinal direction. The horizontal and vertical structures are coupled by the eigenvalues of the vertical structure equation, the so-called "equivalent depth" which is also the mean depth of the linearized shallow-water equations. The reader is referred to (Žagar et al., 2015) and Kasahara (2020) and references therein for details of the theory.

MODES is applied to the four modern reanalyses: ERA5 (Hersbach et al., 2020), ERA-Interim (Dee et al., 2011), the Japanese 55-year Reanalysis JRA-55 (Kobayashi et al., 2015), and the Modern-Era Retrospective analysis for Research and Applications MERRA (Rienecker et al., 2011). We use daily data at 12 UTC from 1980-2014 (1980-2019 for ERA5) on the regular Gaussian grid that consists of  $256 \times 128$  grid points in the zonal and meridional directions, respectively. Vertically the data are interpolated on the predefined 43  $\sigma$  and at time  $t$ , levels.

The projection consists of two steps. In the first step, the 3D data  $\mathbf{X}(\lambda, \varphi, \sigma)$  is expanded into a series of orthogonal vertical structure functions VSFs  $G_m$  according to

$$\mathbf{X}(\lambda, \phi, \sigma) = (u, v, h)^{TT} = \sum_{m=1}^M G_m(\sigma) \mathbf{S}_m \mathbf{X}_m(\lambda, \phi) G_m(\sigma \varphi). \quad (1)$$

The vertical mode index  $(m)$  ranges from 1 (known as the external mode) to  $M$ , the total number of vertical modes, that can be equal or less the number of vertical levels. For every  $m$ , the vector  $\mathbf{X}_m(\lambda, \phi) = (\tilde{u}, \tilde{v}, \tilde{h})^T$  is normalized by the scaling nondimensional data matrix  $\mathbf{X}_m(\lambda, \varphi) = (\tilde{u}, \tilde{v}, \tilde{h})^T$  is obtained by the normalisation by the  $3 \times 3$  diagonal matrix  $\mathbf{S}_m$  with elements  $\sqrt{gD_m}, \sqrt{gD_m}, D_m$ , where  $D_m$  is equivalent depth.

The first seven vertical structure functions (VSFs) are presented in Fig. 1. The external mode ( $m=1$ ) and the subsequent four other modes ( $m=2-5$ ) do not change sign below the tropopause, and are regarded as troposphere-barotropic modes denotes the equivalent depth of the vertical mode  $m$ . The nondimensional variables are defined with  $\tilde{\cdot}$ .

Vertical structure functions (VSFs) for the first seven vertical modes derived using 43 model levels in ERA-Interim. Modes that do not cross zero below the tropopause (here we refer to 250 level) are regarded as barotropic tropospheric modes.

In the second step, for every  $m$ , the horizontal nondimensional motions are projected onto a series of Hough harmonics  $\mathbf{H}_n^k$  with the complex Hough expansion coefficients  $\chi_n^k(m)$ , for every  $m$  as

$$\mathbf{X}_m(\lambda, \phi, \varphi) = \sum_{n=1}^R \sum_{k=-K}^K \chi_n^k(m) \mathbf{H}_n^k(\lambda, \phi, \varphi; m), \quad (2)$$

where  $K$  denotes the total number of zonal waves, and  $R$  denotes is the total number of meridional modes which contains three motions in the atmosphere: Rossby modes, eastward and westward inertia-gravity modes.

The horizontal structure functions (HSFs) are given in terms of the Hough harmonics  $\mathbf{H}_n^k$  which are defined as

$$\mathbf{H}_n^k(\lambda, \phi, m) = \Theta_n^k(\phi, m)e^{ik\lambda},$$

185 with the meridional Hough vector function  $\Theta_n^k = [U_n^k(\phi, m), iV_n^k(\phi, m), Z_n^k(\phi, m)]^T$ , harmonic waves  $e^{ik\lambda}$  in the longitudinal direction with the zonal wavenumber  $k$ , and the The complex Hough expansion coefficients  $\chi_n^k(m)$  depend on three indices:  $m$ , meridional mode index  $n$  for every  $m$ .

Hence, the Hough expansion coefficient,  $\chi_n^k(m)$ , is obtained as

$$\chi_n^k(m) = \frac{1}{2\pi} \int_0^{2\pi} \int_{-1}^1 \mathbf{X}_m(\lambda, \phi) [\mathbf{H}_n^k]^* d\mu d\lambda.$$

## 190 2.2 Total energy of balanced atmospheric circulation

and zonal wavenumber  $k$ . For every  $n$ , the projection includes two types of motions: Rossby modes<sup>3</sup> (quasi-geostrophic or balanced dynamics) and inertia-gravity modes that represent divergence-dominated unbalanced dynamics. The inertia-gravity modes consist of eastward- and westward-propagating solutions and together with the equatorial Kelvin and mixed Rossby-gravity waves constitute the non-Rossby modes that are not used in this study.

195 The first step in the statistical analysis of the Rossby modes It is the inverse of Eq. (1) and Eq. (the balanced circulation) considers the probability distribution of the real and imaginary parts of the Hough coefficients. We find that real and imaginary parts are Gaussian distributed for a single Rossby mode in the synoptic wavenumber range. Since in physical space kinetic energy is the sum of the squares of the horizontal wind components, the distributions of the energy components are approximately  $\chi^2$ -distributed with a distinct non-zero skewness. We do not normalise the coefficients in single modes to unity variance for the  
 200 purpose of retaining the different energy contributions. Thus we do not consider energy distributions as exactly  $\chi^2$ -distributed, but we will assess changes of the skewness during heat waves as an indicator for the changes in the atmospheric circulation. The total energy is given in terms of the real and imaginary parts of the Hough coefficients

$$I_n^k(m) = \frac{1}{2}gD_m|\chi_n^k(m)|^2 = \frac{1}{2}gD_m[(\text{Re}\chi_n^k(m))^2 + (\text{Im}\chi_n^k(m))^2],$$

where  $g$  is the gravitational acceleration and  $D_m$  are the equivalent depths.

205 We consider the extended boreal summer (MJJAS, May-September) during which the major part of heat waves in the mid-latitudes occur.

The energy computed from the daily Hough coefficients is  $I_{d,y}$  with  $d$  denoting the day in MJJAS and  $y$  denoting the year in the datasets. We calculate the climatological mean of the annual cycle

$$\langle I_{d,y} \rangle_y = \frac{1}{N_y} \sum_{y=1}^{N_y} I_{d,y},$$

<sup>3</sup>We use both 'modes' and 'waves' interchangeably but the latter refers to the case without the zonal mean state ( $k = 0$ ).

210 2) that is solved in the forward projection. The second step gives the complex Hough expansion coefficients  $\chi_n^k(m)$  as

$$\chi_n^k(m) = \frac{1}{2\pi} \int_0^{2\pi} \int_{-1}^1 \mathbf{X}_m(\lambda, \varphi) [\mathbf{H}_n^k]^* d\mu d\lambda. \quad (3)$$

for each day in MJJAS (153 in total). The integration in the zonal direction is calculated by the fast Fourier transform and in meridional direction by the Gaussian quadrature.

The energy deviations (or anomalies) from the climatological annual cycle  $\langle I_{a,y} \rangle_y$  are

215  $I' = I - \langle I \rangle_y,$

where  $I$  denotes  $I_{a,y}$  for brevity. At this stage, we form new time series of energy anomalies with time steps of the observed heat waves (Table 1). Then, we compute normalized energy anomalies by

$$\tilde{I}' = \frac{I'(t)}{\sigma}$$

with their climatological standard deviation  $\sigma$ . Note that the entire time series of energy anomalies (climatology) and time series only during heat waves are normalized by different  $\sigma$ .  
 220 projection is carried out using the following truncations:  $K = 100$ ,  $M = 27$ , and  $R = 150$  which combines 50 meridional modes for the Rossby modes, for the eastward inertia-gravity and for westward inertia-gravity waves modes.

This procedure is applied mode-wise for every dataset independently. The next step is to split the normalized energy anomalies of the single Rossby modes into planetary ( $k = 1, 2, 3$ ) and synoptic ( $k = 4 - 10$ ) intervals, and then to average  
 225 only the troposphere-barotropic modes  $m = 1 - 5$  within these intervals. The zonal flow is given by  $k = 0$ . In each case, all meridional modes are averaged except for the first one, which corresponds to Since the mixed Rossby-gravity mode and is counted among the balanced modes in MODES software.

Lastly, we combine all reanalyses in the above-mentioned atmospheric flows. Žagar et al. (2020) showed that the differences between climatological energy spectra for the four reanalyses are minor. Therefore, our PDFs consist of independent but similar  
 230 time series. Thus, we can detect robust features of distributions of energy anomalies across different datasets. is counted as the first balanced modes, we have 49 Rossby modes for every  $m$  and  $k$ , so that the meridional mode index goes from  $n = 1$  to  $n = 49$ .

We are interested in the balanced circulation with the troposphere-barotropic vertical structure that characterises the midlatitude weather during heat waves. As shown in Fig. 1, the first five VSFs do not change their signs below the tropopause (taken at  
 235 250 hPa), and can therefore be regarded as troposphere-barotropic modes.

## 2.2 Data

### 2.2 Heat Waves

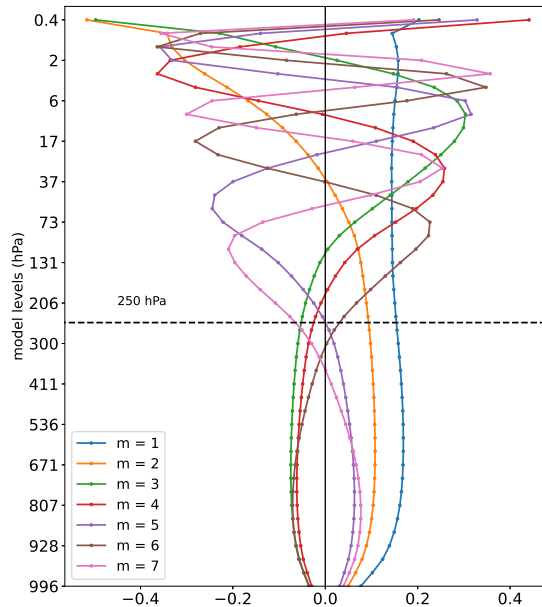


**Figure 1.** Vertical structure functions (VSFs) for the first seven vertical modes. VSFs are derived for 43  $\sigma$  levels using the stability profile of ERA-Interim data. VSFs that do not change the sign below the tropopause (defined as 250 hPa level) are troposphere-barotropic modes.

To reduce statistical uncertainty, we project four reanalyses: ERA5 (Hersbach et al., 2020), Era-Interim (Dec et al., 2011), the Japanese 55-year Reanalysis JRA-55 (Kobayashi et al., 2015), and the Modern-Era Retrospective analysis for Research and Applications MERRA (Rienecker et al., 2011). We use daily data at 12:00 UTC from 1980-2014 (1980-2019 for ERA5) on 256  $\times$  128 grid points in the zonal and meridional directions, respectively. We interpolate this data on the predefined 43  $\sigma$  levels. After the NMFs projection to modal space, we obtain the daily time series of Hough coefficients with the following truncations:  $K = 101$ ,  $M = 27$ ,  $R = 150$ , where  $M$  denotes the number of vertical modes and  $K$  includes the zonal mean flow ( $k = 0$ ).  $R$  combines equal numbers of meridional modes ( $n = 50$ ) for the Rossby modes, eastward inertia-gravity modes and westward inertia-gravity waves modes.

We analyse heat waves for the Eurasian region limited by the Ural mountains [ $35^{\circ}N - 65^{\circ}N, 10^{\circ}W - 60^{\circ}E$ ]. The choice of the [ $35^{\circ}N - 65^{\circ}N, 10^{\circ}W - 60^{\circ}E$ ]. The study area is defined by capturing the most significant atmospheric processes occurring during heat waves frequently affected by heat waves (e.g., Zhou and Wu, 2016), in particular, Eastern Europe and Western Russia, a region of one of the strongest heat waves observed in recent decades (e.g., Barriopedro et al., 2011). For heat wave identification, we analyse daily 2 m temperature fields for the extended boreal summer (MJJAS) from 1980-2014 (until 2019 for ERA5). The identification algorithm applied by Ma and Franzke (2021) uses the following two criteria: (i)

the temperature exceeds the 95th percentile threshold and (ii) the duration of the exceedance is larger than three consecutive time steps. As the identification algorithm is performed for each reanalysis, it is expected to have discrepancies among them. Therefore, we form a list of heat waves as a list of physically consistent extreme events. We find that the total number of days with heat waves affects the statistical significance of results in modal space. When the results of the identification algorithm are more precise within the list of heat waves, the results of the statistical analysis in modal space are less significant due to the small sample size. Table 1 presents the list of days with heat waves in reanalysis datasets, which is formed on the basis of the preconditions based on the algorithm mentioned above.

### 2.3 Time series of Rossby wave energy anomalies

The total (kinetic plus available potential) energy of a single mode  $\nu = (k, n, m)$  is given by the square of the absolute value of the Hough coefficient (i.e. in terms of its real and imaginary parts) as

$$I_\nu = I_n^k(m) = \frac{1}{2}gD_m \left| \chi_n^k(m) \right|^2, \quad (4)$$

where  $g$  is the gravity. See Kasahara (2020) for the derivation of Eq. (4).

The time series of the daily total energy is denoted  $I_\nu(t)$  span over the period of extended boreal summer (MJJAS, May-September) within 35 years (1980-2014) for ERA-Interim, JRA-55, MERRA ( $N_y = 35$ ) and 40 years (1980-2019) for ERA5 ( $N_y = 40$ ). The climatological annual cycle is obtained as an average over all years ( $N_y$ ) for each day in MJJAS as

$$\langle I_\nu \rangle = \frac{1}{N_y} \sum_{y=1}^{N_y} I_{\nu,y}, \quad (5)$$

and subtracted from daily energies to compute the energy deviations (or anomalies) as

$$I'_\nu = I_\nu - \langle I_\nu \rangle. \quad (6)$$

The time series of  $I'_\nu$  define the climatology.

At this stage, we form also the time series of energy anomalies with time steps of the observed heat waves according to Table 1. Although only 13 heat waves are identified in ERA-Interim, JRA-55 and MERRA due to the shorter datasets, we include them to increase the sample size. We note that all 13 heat waves are identified in all reanalyses, but the individual datasets differ, as can be inferred from the number of detected days. Thus, we consider them as different realizations. We normalize energy anomalies by their climatological standard deviation  $\sigma_\nu$ .

$$\tilde{I}'_\nu = \frac{I'_\nu}{\sigma_\nu}. \quad (7)$$

The mode-wise normalisation by the standard deviation is crucial since the energy spectrum is red not only in terms of the horizontal scales (Žagar et al., 2017), but also the vertical scale. Note that the entire time series of energy anomalies

**Table 1.** Heat waves in Eurasia during May-September 1980-2019

		ERA5	ERA-Interim	JRA-55	MERRA
	Start date	Number of detected days			
1	1994-09-23	3	3	2	3
2	2006-06-18	12	10	12	10
3	2006-09-20	3	5	6	2
4	2007-05-20	12	12	12	12
5	2007-08-21	6	6	6	6
6	2008-09-05	4	3	4	3
7	2010-06-28	26	27	27	26
8	2010-07-27	21	21	19	21
9	2012-05-09	4	4	4	4
10	2012-06-14	4	3	4	3
11	2013-05-02	7	7	6	5
12	2014-05-17	5	3	3	3
13	2014-06-05	5	6	5	6
14	2015-06-02	3	-	-	-
15	2015-08-11	3	-	-	-
16	2015-09-17	11	-	-	-
17	2016-06-21	4	-	-	-
18	2016-08-20	9	-	-	-
19	2018-05-02	8	-	-	-
20	2018-06-27	4	-	-	-
21	2018-07-13	22	-	-	-
22	2018-08-29	7	-	-	-
23	2018-09-11	12	-	-	-
24	2019-06-01	3	-	-	-
25	2019-06-08	5	-	-	-
26	2019-06-18	3	-	-	-
27	2019-06-23	4	-	-	-
28	2019-07-24	3	-	-	-
$\sum$ N-of days		213	110	110	104

(climatology) and time series during heat waves are normalized by different  $\sigma$ . This procedure is applied for every reanalysis dataset independently.

The next step is to split the normalized energy anomalies of the single Rossby modes into planetary ( $k = 1 - 3$ ) and synoptic ( $k = 4 - 10$ ) intervals, and then to average over the troposphere-barotropic modes  $m = 1 - 5$  within these intervals. The mean zonal flow is given by  $k = 0$ . For each  $k$ , averaging is applied also over meridional modes whenever the results are discussed in terms of a single modal index.

285 Finally, we combine the time series of normalized energy anomalies in the above-mentioned wavenumber ranges. Žagar et al. (2020) showed that the differences between climatological energy spectra for the four reanalyses are minor. Therefore, our PDFs consist of independent but similar time series. Thus, we can detect robust features of distributions of energy anomalies across different datasets.

### 3 Results

290 First, we confirm Fig. 2 demonstrates that the global energy in a single Rossby mode is  $\chi^2$ -distributed using the climatology from 1980-2014. In our example, we use the energy (Eq. 4) of the balanced mode with  $k = 7$ ,  $n = 3$  associated with a significant part of mid-latitude circulation, and  $m = 1$  Rossby mode with  $(k, n, m) = (7, 3, 1)$  which is associated with variability in midlatitude barotropic circulation. The histogram and the fit of the  $\chi^2$ -distribution with two degrees of freedom,  $df = 2$ , corresponding correspond to the real and the imaginary parts is shown in Fig. 2 of the time series of  $I_n^k(m) = I_3^7(1)$ . The Kolmogorov-Smirnov test reveals a negligible  $p$ -value, confirming the fit. Therefore, we find that approximation of  $\chi^2$ -distributed energy is satisfied to a high degree, as expected.

295

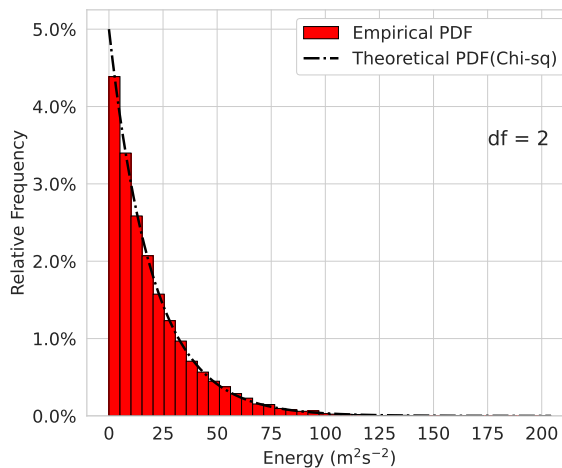


**Figure 2.** Atmospheric energy (empirical) distribution in the Rossby (balanced) regime wave with zonal wavenumber ( $k = 7$ ), meridional mode ( $n = 3$ ) and vertical index ( $m = 1$ )  $m = 1$  for 1980-2014. The dashed black lines correspond to the theoretical ( $\chi^2$ ) distribution ( $df$  are the degrees of freedom).

### 3.1 Northern Hemisphere ~~extratropical-midlatitude~~ circulation ~~decomposition~~ during heat waves

~~We present the decomposition of the climatological Rossby circulation and case studies for~~ In this section, we demonstrate that the selected subset of vertical modes is suitable for the statistical analysis by demonstrating the climatological circulation and two selected heat wave events. ~~Here, we show only with applied filtering. We show the ERA5 results because other datasets demonstrate, but other datasets provide~~ similar results. Figure 3a depicts the May-September balanced circulation (Rossby modes with  $k > 0$  and all  $m, n$ ) at a single  $\sigma$  ~~level-level~~ close to 500 hPa. The pattern remains almost the same when we restrict vertical modes to only the troposphere-barotropic modes,  $m = 1 - 5$   ~~$m = 1 - 5$~~  (Fig. 3b). ~~Thus~~ This confirms that our selection of modes is suitable for ~~the purpose of analysing~~ analyzing the troposphere-barotropic circulation, i.e. the ~~pattern~~ patterns observed during surface extreme events ~~and often referred to as “atmospheric blocking”, commonly associated with the blocking.~~

This structure is clearly recognized when we reconstruct circulation during two recent extreme heat events: the Russian Heat Wave in 2010 (Barriopedro et al., 2011) and the European Heat Wave in 2019 (Xu et al., 2020). The difference with respect to climatology which is presented in Fig. 3b. In both cases, we observe strong positive anomalies over the locations of the observed surface extremes (Western Russia and Europe) with nearby negative anomalies. For the Russian Heat Wave in Fig. 3c, d, the anomalies over Central and Southern Asia reveal cyclones which have produced extreme rainfall known as the Pakistan Flood (~~?~~) (Lau and Kim, 2012). Furthermore, the wavy pattern along the latitudinal belt depicts teleconnections (Teng and Branstator, 2019). The plots with the difference between climatology and each heat wave (Fig. 3d,f) demonstrate the meridional extension of the waves from polar to tropical regions confirming the impact of these regions on ~~mid-latitude~~ midlatitude extremes (Behera et al., 2012). ~~While the patterns shown in Fig. 3 are qualitatively known from previous studies, our result was obtained by a novel method that allows a scale-dependent quantification of the associated circulation with respect to the global climatology. This result also justifies our use of the subset of vertical modes in the statistical analysis presented below.~~

### 3.2 Statistics in modal space

The ~~decomposition example~~ in the previous section demonstrated how the Rossby circulation ~~modified during~~ is altered regionally during Eurasian heat waves. Our next step is to ~~understand what the heat waves signatures in the global variability spectrum are and, therefore, investigate how these heat waves affect (if) the global spatial variability spectrum, i.e. their impact on global atmospheric circulation. Under the circulation. Here, the term~~ global variability spectrum, ~~we imply refers to~~ the PDFs of the ~~global energy anomalies and under signatures~~ normalized anomalies in global energy, and the effects (or signatures) of heat waves, ~~we imply implies~~ significant changes in the ~~distributions~~ distribution of energy anomalies. As a first step, we ~~analyse analyze~~ the climatological PDFs ~~of the normalized energy anomalies of modes with in terms of~~ zonal wavenumbers corresponding to three ~~intervals-ranges~~ as described in Section 2 ~~with emphasis on the skewness~~: (i) the zonal mean state,  $k = 0$ , (ii) the planetary-scale circulation  $k = 1 - 3$ , and (iii) the synoptic-scale circulation with  $k = 4 - 10$ . ~~We focus on the skewness which is not impacted by the normalization.~~

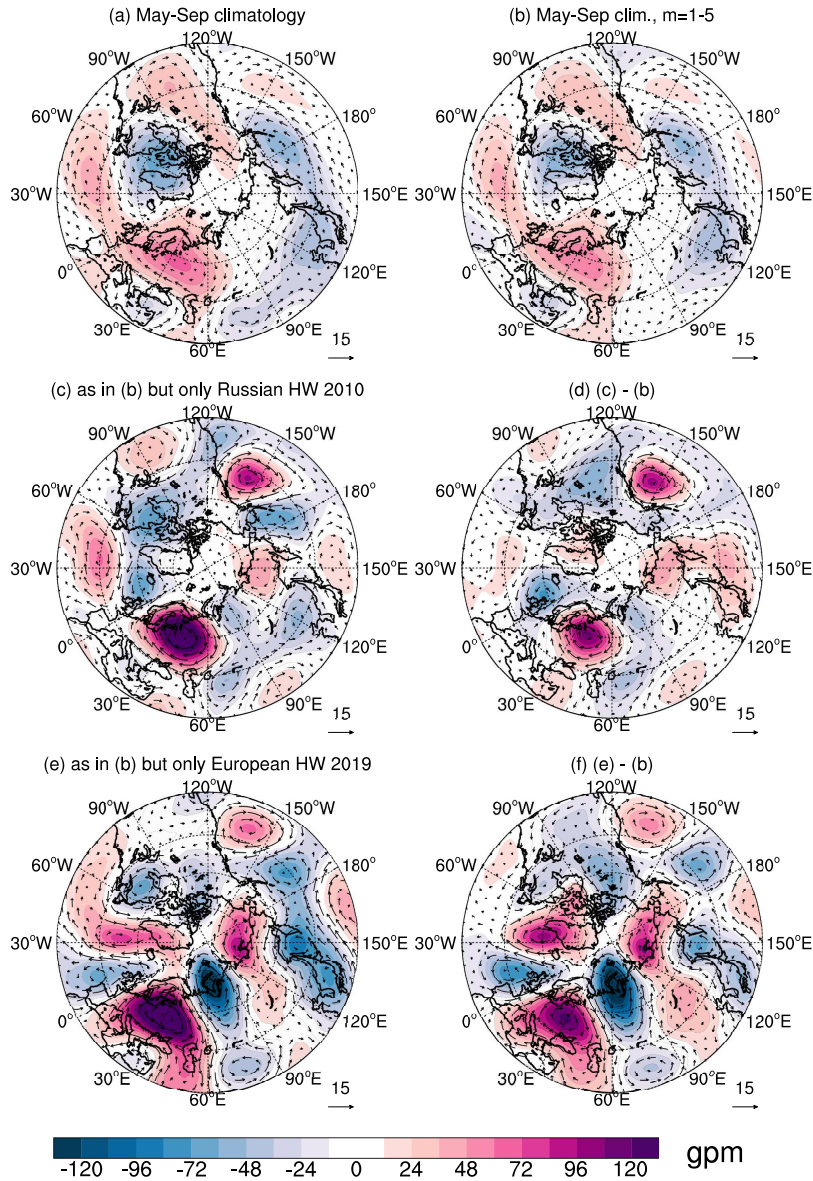


**Figure 3.** Climatological **balanced-circulation** (Rossby **modes for  $k > 0$** ) **wave circulation** for extended boreal summer (**MJJAS**) at a **terrain-following**  $\sigma$  level close to 500 hPa (ERA5 model level 30) in the **mid-latitudes-midlatitudes** ( **$35^{\circ}N - 65^{\circ}N$** ). Coloured contours are geopotential height anomalies (in gpm) for Rossby **modes-waves** and (a) **including all** zonal wavenumbers  **$k > 0$**  (**no zonal mean state**), **all** meridional modes  **$n$**  and **all** vertical **structure-functions**. **The zonal mean state ( $k = 0$ ) is not included** modes  **$m$** . (b) as in (a), but only troposphere-barotropic vertical modes **are included** ( **$m = 1 - 5$** ),  **$m = 1 - 5$** , (c) as in (b) but for the Russian Heat Wave (HW) in 2010. (d) Difference between the (c) and (b). As in (c), (e, f) illustrate Rossby **circulation-waves** during **the** European Heat Wave (HW) 2019. Wind speed is shown by the length of the wind vectors (15 m/s<sup>-1</sup> as a reference vector).

330 Figure 4a shows the PDF of the total Rossby circulation which with all zonal wavenumbers included in the analysis. With the skewness equal to 0.38, the PDF clearly deviates from a Gaussian distribution. The PDFs of the planetary-scale (Fig. 4c) and the synoptic-scale (Fig. 4d) Rossby waves PDFs also do not follow a normal distribution, but exhibit noticeable asymmetry, with the planetary-scale skewness almost twice greater than the one of the synoptic-scale Rossby waves.

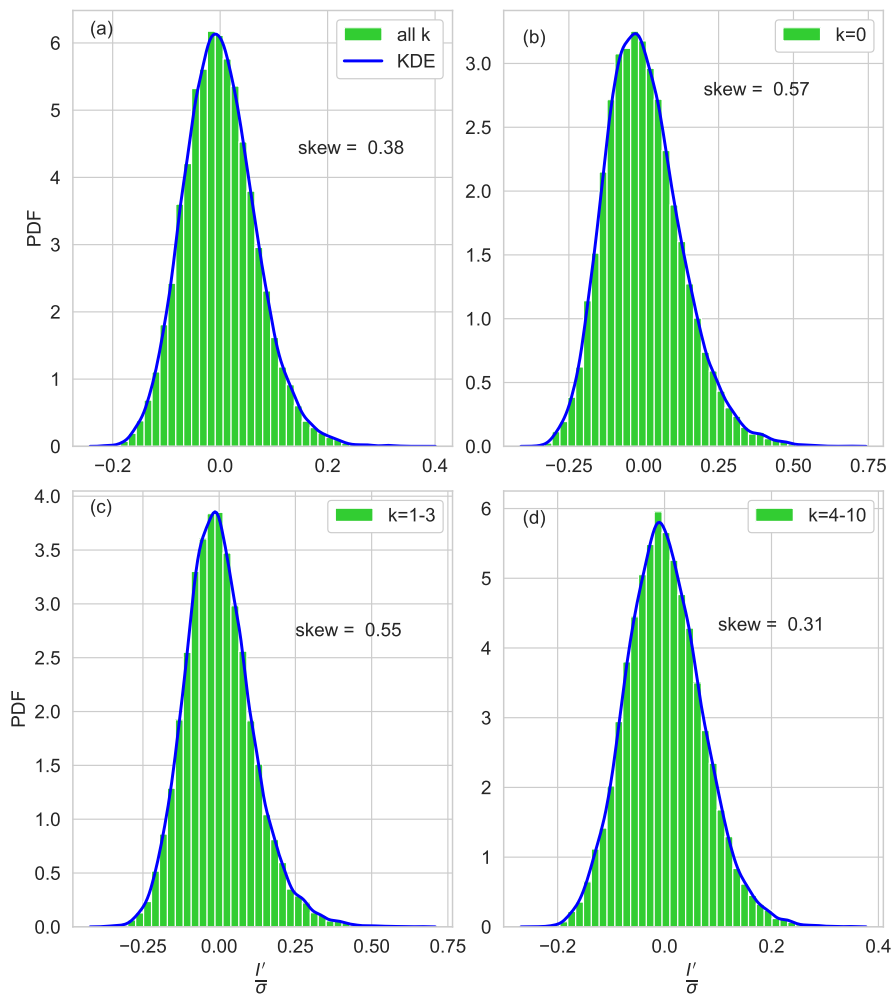


**Figure 4.** PDFs of normalized total energy anomalies (all  $k$ ), (b) the zonal mean state ( $k=0$ ), (c) planetary-scale waves ( $k=1-3$ ), (d) synoptic-scale waves ( $k=4-10$ ). Empirical PDFs are depicted as green bars for extended boreal summer (MJJAS) 1980-2014 (1980-2019 for ERA5). The blue curve is the Kernel Density Estimator (KDE).

335 To determine this asymmetry, we consider the skewness of the PDFs for examined flows and all in Fig. 4 is based on the four reanalyses (ERA5, ERA-I, JRA-55, MERRA) combined. For a more robust statistical analysis, we apply bootstrapping with a replacement which results in an agreement between considered datasets - all values for different wavenumber ranges for

a more robust statistical analysis (Fig. 5). Note that all values from reanalysis datasets are within the defined 95% confidence intervals (CI) presented as horizontal lines at the ends of bars (Fig. 5a) for each wavenumber range (here is not shown). The bootstrapped skewness shows that the normalized energy anomaly distribution has the highest asymmetry in the planetary scales and zonal mean circulation which is also detected as stretched right tails in the PDFs. The different skewnesses in the four wavenumber ranges can partly be explained by varying degrees of freedom. For the latter, we refer to the number of single modes within the mentioned can partly explain the different skewnesses in the four wavenumber ranges. However, changes in the dynamics can modify the skewness and the active degrees of freedom, and this which is addressed in the next section.

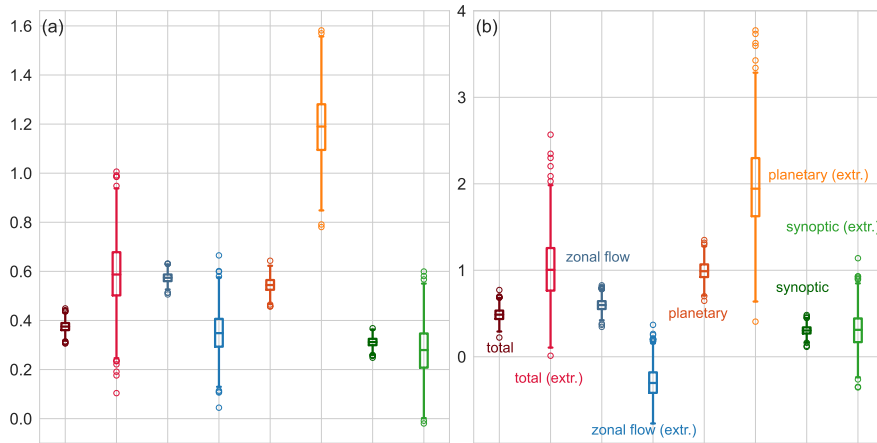


**Figure 5.** Box-plots for (a) skewness and (b) excess kurtosis of normalized energy anomalies distributions for four considered atmospheric components: total Rossby regime with dark- and light-red bars, the zonal mean flow as dark- and light-blue bars, planetary waves as orange and yellow, and the synoptic circulation as dark- and light-green 95%-confidence intervals are obtained through bootstrapping with replacement with 1000 simulations.

345 ~~The same as in Fig. 4 but with normalized energy anomalies only during heat waves presented in Table 1.~~

### 3.2.1 Surface extremes and energy statistics

As a second step, we calculated the energy anomalies. Now we compare PDFs during observed heat waves over Eurasia (28 events in total, see the methods section) and compare it with climatology for different parts of wavenumber space. For comparison, we consider two statistical moments, skewness and excess kurtosis, to diagnose the changes in shape, especially in the tails of distributions for the four reanalyses datasets. We find that only the difference in the skewness of the planetary-scale distribution is statistically significant, i.e the bootstrapped values are outside CIs of climatological bootstrapped skewness only during extremes.

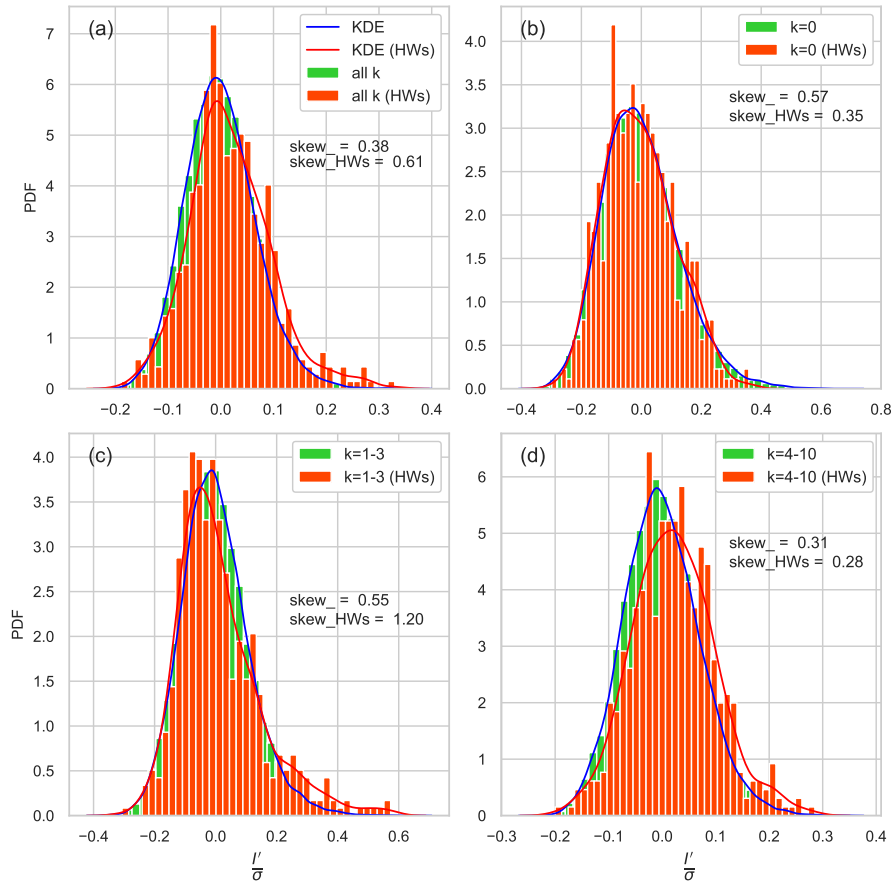


**Figure 6.** [The same as in Fig. 4 but with normalized energy anomalies only during heat waves \(HWs\) presented in Table 1.](#)

The PDFs of the normalized energy anomalies depicted in Fig. 6 demonstrate how probabilities of the energy deviations change during surface extreme events. First, there is a positive shift in the mean except for  $k = 0$ , and, as a consequence, an increased probability of intermediate positive deviations.

According to Fig. 5a, the change in the skewness, which is considered as the main indicator, is the largest for the planetary-scale circulation. The excess kurtosis for extreme events is approximately twice larger than climatology (Fig. 5b), which reflects a drastic rise in the probability of extreme values. The opposite change is found for the zonal mean flow during surface heat waves, where skewness and the excess kurtosis decrease; this implies that the distribution becomes flatter with thinner tails and is less extreme. Based on this, we conclude that the amplitudes of the planetary circulation amplify as shown in Fig. 3d, f, while the zonal mean flow anomalies become weaker in agreement with [Coumou et al. \(2015\)](#) [Coumou et al. \(2014\)](#). Thus, we have evidence that signatures of heat waves are seen in different parts of the global variability spectrum via statistically significant changes in skewness.

The increase in skewness allows for the estimation of the reduction of the active ~~dynamical~~ degrees of freedom during  
365 the heat waves compared to the climatological mean. For the estimation, we use the exact relation for the skewness of  $\chi^2$ -  
distributed variable,  $\gamma = \sqrt{8/df}$ , ~~with sums of where  $df$  as is the number of~~ squares of the independent Gaussian variables with  
~~unit variance. We are not able to derive the absolute values in our analysis since this would require identifying the independent~~  
~~degrees of freedom in the set of modes, which is beyond the aim of the present study. (An estimation of absolute numbers of~~  
~~degrees of freedom using a unit variance which defines~~ the  $\chi^2$ -distribution in geopotential height fields was presented in ?.)  
370 ~~-distributed variable.~~

~~However, we can derive~~ We use the ratio  $df_e/df_c = \gamma_c^2/\gamma_e^2$ , ~~where  $df_e$  is which says that the ratio between~~ the number of  
~~active~~ degrees of freedom during ~~extreme events heat waves and climatology,  $df_e$~~  and  ~~$df_c$  is the number of degrees of freedom~~  
~~in climatology with the skewness, is equal to the ratio of their skewnesses  $\gamma_e$  during extremes and the climatological mean~~  
~~and  $\gamma_c$ , respectively.~~ The rough estimates  $\gamma_e \approx 1.2$  and  $\gamma_c \approx 0.6$ , based on Fig. 5a, yield a reduction of the ~~active~~ degrees of  
375 freedom of the order of  $df_e/df_c \approx 1/4$  during the extreme events.

~~Since the projection in modal space is global, it is worthwhile to separate the entire atmosphere into symmetric and~~  
~~asymmetric components. The symmetry is defined~~ Unlike the change in skewness in the PDFs of the planetary Rossby  
~~waves, there is a statistically significant change (according to the Mann-Whitney U test with 95%-confidence) in the entire~~  
~~PDFs of synoptic Rossby waves. The change can be seen in a distribution shift toward positive energy anomalies (figure~~  
380 ~~not shown), which can be interpreted as more energy is expected at synoptic scales during heat waves. More intensive~~  
~~cyclones and anticyclones are found to maintain blocking throughout eddy straining (Shutts, 1983) and selective absorption~~  
~~(Yamazaki and Itoh, 2013) mechanisms.~~

Finally, we make a note on the fact that the changes in PDFs during the Eurasian heat waves apply to the global atmosphere.  
~~Our Rossby modes consist of symmetrical ( $n$  odd) and asymmetrical ( $n$  even) components with symmetry~~ with respect to the  
385 equator ~~defined~~ for the geopotential height and zonal wind fields. ~~By considering symmetric and asymmetric modes, we find~~  
~~that both~~ We checked that both symmetrical and asymmetrical parts contribute to ~~changes in the energy anomalies distribution.~~  
~~This means that~~ the PDFs of all meridional modes. In other words, the Rossby waves in the Southern Hemisphere might have  
contributed to the results presented ~~here for the Northern Hemisphere heat waves. Taking.~~ However, taking into account the  
lower frequency of atmospheric blocking (~~symmetric part~~) (Wiedenmann et al., 2002) in the Southern Hemisphere, we may  
390 assume that this influence is negligible. ~~We also find that the Southern Hemisphere cyclones (asymmetric part) do not show~~  
~~significant change during the Northern Hemisphere heat waves.~~

### 3.3 Changes in the ~~extratropical midlatitude barotropic~~ circulation during ~~the~~ heat waves

~~Atmospheric Rossby circulation filtered in physical space (only  $k = 1-3, n = 2-50, m = 1-5$ ) at the  $\sigma$ -level close to 500~~  
~~in ERA5. Coloured contours are geopotential height anomalies, spaced by 20, wind speed is shown by the arrow length.~~  
395 (a) Mean circulation in May-September obtained in the 40-year climatology (1980-2019), (b) composite of 28 Eurasian Heat  
Waves (HWs) presented in Table 1, (c) is the difference between (b) and (a). (d) Mean vertical profile at  $54^\circ N$ , (e) the same as

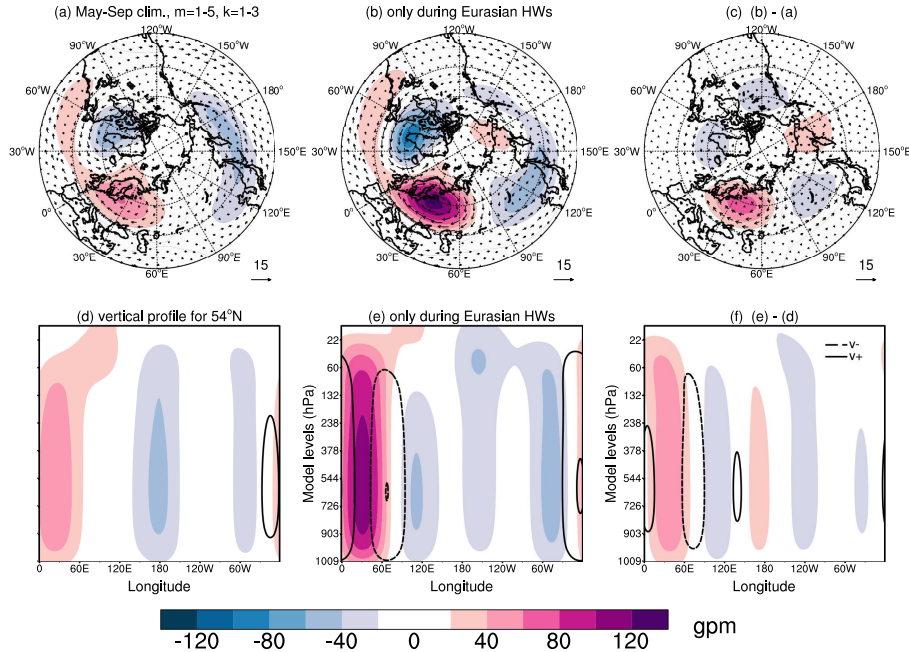


**Figure 7.** Planetary-scale, troposphere-barotropic Rossby waves ( $k = 1 - 3$ ,  $m = 1 - 5$ , all  $n$ ) at the  $\sigma$ -level close to 500 hPa in ERA5. Coloured contours are geopotential height anomalies, every 20 gpm. The wind speed is shown by the arrow length. (a) Mean circulation in May-September obtained in the 40-year climatology (1980-2019), (b) composite of 28 Eurasian Heat Waves (HWs) presented in Table 1, (c) difference between (b) and (a). (d) Climatological geopotential height perturbations (coloured isolines) in planetary scales along 54°N, (e) As in (d) but during HWs, (f) difference between (d) and (e). Solid and dashed contours in (d)-(f) show the planetary-scale meridional winds (northward and southward, respectively) every 2  $\text{ms}^{-1}$ .

~~(d) only during heat waves, (f) is the difference between (e) and (f). Solid and dashed contours illustrate the meridional wind (northward and southward, respectively) every 2-~~

The next step is to relate the ~~results to anomalies in PDFs of energy anomalies in large-scale circulation with~~ physical space. This is achieved by filtering the analyzed Rossby modes ( ~~$k = 1 - 3, m = 2 - 50, m = 1 - 5$~~   $k = 1 - 3, n = 1 - 49, m = 1 - 5$ ) to physical space, similar to what has been done in Fig. 3. Instead of case studies, ~~we demonstrate the Rossby now we present the~~ circulation averaged over all days with observed extremes. ~~We show again As earlier, we show~~ the horizontal circulation at ERA5  $\sigma$ -level near 500 hPa as representative for the troposphere-barotropic circulation.

Figures 7b and c reveal an enhancement of positive height anomalies in the eastern part of the Baltic Sea and negative anomalies over the North Atlantic. Moreover, one can notice a north-westward shift of negative anomalies in the Asian part compared to climatology presented in Fig. 7a and the formation of positive anomalies over Chukotka and Alaska. According to Fig. 7c, the dominant patterns are zonal wavenumber 2 and 3.

Figures 7d,e show the vertical profile for  $54^{\circ}N-54^{\circ}N$  of the meridional wind speed and the geopotential height anomalies for climatology, during heat waves. Figure 7f depicts the difference between two profiles. We illustrate again that the structure is barotropic over the entire troposphere and lower stratosphere, as was observed in some studies. Moreover, there is an enhancement of northward winds over Europe ( $0^{\circ}E-30^{\circ}E$   $0^{\circ}E-30^{\circ}E$ ) and southward winds over the Asian part of Russia ( $60^{\circ}E-90^{\circ}E$   $60^{\circ}E-90^{\circ}E$ ) with southerlies over the Kamchatka Peninsula (Fig. 7f). Overall, we find an increase in wave amplitudes, and change in phases as can be noticed by west- and northward shifts in Fig. 7b, c and Fig. 7d, e in the Baikal lake area ( $90^{\circ}E-120^{\circ}E$ ). According to Teng and Branstator (2012) and Ragone and Bouchet (2021), the wave-3 pattern is dominant for heat waves that occurred in the US, France and Scandinavia. Therefore, the results ~~agree with previous studies and demonstrate how surface extremes modify atmospheric circulation~~ demonstrate how atmospheric circulation is changed during surface extremes not only locally but also in remote regions, similar to the idea of teleconnection patterns noted in recent studies (e.g., Kornhuber et al., 2019).

### 3.4 Heat waves in submonthly Rossby wave Intramonthly variance spectra and entropy reduction during the heat waves

So far, we showed signatures of ~~extremes heat waves~~ in spatial variance. ~~In contrast to the spatial variance (energy) spectra, temporal variance spectra are not well studied.~~ Žagar et al. (2020) analyzed subseasonal variance and showed its. Now we look at changes in temporal variance due to extremes and couple it to the changes in entropy which measures the average uncertainty with which one knows the state of the system. The temporal variance and its square root, variability, are usually studied locally or using the time series of atmospheric indices such as North Atlantic Oscillation. The global intraseasonal variance in the reanalysis data was analyzed by Žagar et al. (2020) who showed statistically significant trends in planetary and synoptic scales both midlatitude Rossby waves and large-scale equatorial waves. Here, we carry out a similar analysis for submonthly scales. Unbiased submonthly variance ( $\bar{V}_\nu$ ) is computed as focus on intramonthly scales associated with heat waves with the unbiased variance ( $Jkg^{-1}$ ) computed as

$$V_\nu = \frac{1}{N-1} \sum_{t=1}^N \underline{gDgD}_m \left| \chi_\nu(t) - \bar{\chi}_\nu \right|^2, \quad (8)$$

where  $\bar{\chi}_\nu - \bar{\chi}_\nu$  is the monthly mean and  $N$  is the number of days in a single month. Zonal wavenumber variance spectra are obtained by summing over the vertical modes,  $m=1-5$ , and all meridional indices, except the first one, as As the 3D NMF expansion is a complete representation of the system, the components  $\nu$  of the state vector are statistically independent and correspond to independent degrees of freedom, as discussed in Section 2. The relative change in variance during heat waves is thus

$$V_k = (2 - \delta_{k0}) \sum_{n=2}^{50} \sum_{m=1}^5 V_\nu \frac{(V_\nu - V_\nu^h)}{V_\nu} \quad \text{or} \quad 1 - \frac{V_\nu^h}{V_\nu}, \quad (9)$$

where  $\delta_{k0} = 0$  for  $k > 0$  and  $\delta_{k0} = 1$  for  $k = 0$   $V_\nu^h$  is the intramonthly variance during the heat waves. To obtain the mean state, we average computed variances over all months (May-September) and years (1980-2019) variances are averaged over

months May to September and years 1980 to 2019 in ERA5. ~~To consider only~~ For extremes, we ~~select variances within~~ consider  
 440 ~~intramonthly variances for~~ months with observed heat waves. ~~Zonal wavenumber variance spectra of~~  $V_\nu$  and  $V_\nu^h$  are obtained  
 by ~~summing over the five barotropic vertical modes and over all meridional indices of the Rossby waves.~~

The entropy,  $\mathcal{H}$ , which measures the average uncertainty of the system, is defined as

$$\mathcal{H}(\mathcal{P}) = \int_{R^n} \mathcal{P}(\mathbf{x}) \ln(\mathcal{P}(\mathbf{x})) d\mathbf{x}, \quad (10)$$

where probability density  $\mathcal{P}(\mathbf{x})$  represents the uncertainty of the state  $\mathbf{x}$  of the system. The change in entropy can be described  
 445 by the difference in entropy between the heat wave and climatological probability densities that are represented by diagonal  
 matrices  $\mathbf{Q}^h$  and ~~then average for every mode separately.~~ The result is presented  $\mathbf{Q}$  with entries equal to  $V_\nu^h$  and  $V_\nu$ , respectively  
 (Rogers, 2000). The change can be shown to be

$$\Delta\mathcal{H}(\mathcal{P}) = \mathcal{H}(\mathcal{P}^h) - \mathcal{H}(\mathcal{P}) = \frac{1}{2} \ln \det(\mathbf{Q}^h) - \frac{1}{2} \ln \det(\mathbf{Q}) = \frac{1}{2} \ln \det(\mathbf{Q}^h \mathbf{Q}^{-1}). \quad (11)$$

The results are summarized in Fig. 8. ~~Submonthly variance reduces in~~  $k=3$  First we discuss the intramonthly variance  
 450 spectra shown in Fig. 8a. The overall red spectrum makes it hard to notice that scale-dependent differences, but they are made  
 clear by zooming in the planetary and synoptic scales displayed as an inset panel. It shows a variance reduction of about 6% in  
 the zonal wavenumber  $k=3$  along with the ~~increase in~~  $k=7,8$ . ~~The change is consistent with the idea of circulation blocking~~  
~~during the extreme heat events on submonthly time scales.~~ ~~These results complement the statistical analysis in previous sections~~  
~~that showed significant energy growth on planetary scales in normalized energy anomalies.~~ ~~The two statistical metrics describe~~  
 455 ~~different dynamics, spatial and temporal variance that are coupled through the properties of~~ 5% variance increase in  $k=7-8$ .  
 The blue shading around the variance spectra depicts the 95%-CI obtained through bootstrapping of intramonthly variances.  
 The largest uncertainty is at zonal wavenumbers for the planetary Rossby waves and it shows that the variance reduction at  
 $k=3$  is within 95%-CI and, therefore, is insignificant. The opposite is found at  $k=7-8$ , where the change in the intramonthly  
 variance during heat waves is significant.

Figure 8a however does not include the mean zonal state. A more detailed view of the ~~mean state~~ (~~Žagar et al., 2020~~) changes  
 460 in the global intramonthly variance in comparison with entropy is provided in other two panels. The variance reduction (Fig.  
 8b) and the entropy reduction (Fig. 8c) are qualitatively very similar; they both show a decrease in  $k=3$  along with an increase  
 in  $k=7-8$ . They also agree about the largest variance and entropy changes being in the zonal mean state with a positive and  
 negative change in the two asymmetrical meridional modes,  $n=4$  and  $n=6$ , respectively.

The change in  $k=0$  during Eurasian heat waves can be associated with physical space using the latitudinal structure of the  
 465 Hough functions<sup>4</sup>. But, perhaps even more insightful is the latitudinal profile of the zonal-mean zonal wind presented in Fig.  
 9. Figure 9 shows that the maximum zonal-mean zonal wind at 45°N during heat waves is weaker (about 10%) with respect  
 to climatology and slightly shifted (about 1°) northward. The wind maximum is also better confined within the troposphere,  
 with the 10 ms<sup>-1</sup> isoline at level close 300 hPa compared to level close 200 hPa in climatology. The barotropicality of the

<sup>4</sup>The latitudinal profiles of the Hough functions for the Rossby waves with  $n=1-4$  are available at <https://modes.cen.uni-hamburg.de/Hough>.

470 midlatitude atmosphere near 45°N, as defined by the VSFs not changing the sign below 250 hPa but still supporting the vertical shear of the mean zonal wind, is decreased during the Eurasian heat waves. Another features of the heat waves are twice stronger zonal-mean zonal winds in higher latitudes between 60°N and 90°N with a peak difference of up to 3 ms<sup>-1</sup> at 75°N. The dipole shape of the difference in Fig. 9c is in Hough space of Fig. 8b,c seen as an entropy decrease in  $n = 4$  and an increase in  $n = 6$ . Note that Fig. 9 is obtained by filtering to physical space the  $\bar{\chi}_n^0$  and that similar filtering for any horizontal or vertical scale of interest is straightforward making the holistic modal-space statistics an attractive global complement to the single-variable, single-level Fourier analysis. We speculate that the enhancement of high latitude  $k = 0$  zonal winds is a component of more-persistent double jets over Eurasia during heat waves discussed by Rousi et al. (2022).

475

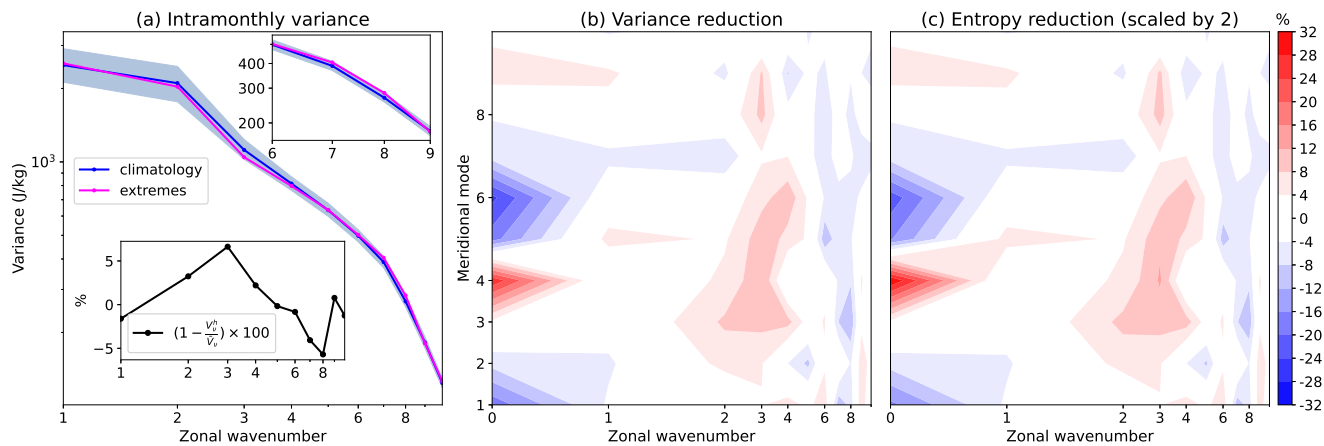


**Figure 8.** a) Time-averaged submonthly-intramonthly variance spectra of the Rossby waves as a function of the zonal wavenumber  $k$  with  $n = 2 - 50$  for climatology (blue line) and  $m = 1 - 5$  Eurasian heat waves (magenta line). Averaging is performed over a 40-year period 1980-2019 (blue line) only, months May-Sep with of ERA5 used as input data. The magenta line depicts energy and variance averaged only during heat waves embedded figure includes (listed in Table 1 bottom left) - The embedded figures include the percentage of relative change and (top right) zoomed spectra for  $k = 6 - 9$ . The 95%-confidence intervals (blue shading) are obtained through bootstrapping with replacement with 1000 simulations. b) Reduction in the intramonthly variance as a function of the zonal wavenumber starting with the zonal mean state. c) As in b), but the reduction in entropy multiplied by a factor of 2.

## 4 Conclusions

480 Extreme events like heat waves at the surface are accompanied by changes in atmospheric circulation across scales. Our study shows that extremes create a fingerprint Eurasian heat waves have signatures in the global circulation. Evidence for the The changes in global statistics of the Rossby wave variance is searched in are made evident by analyzing the four modern reanalyses: the ERA5, ERA-Interim, JRA-55, and MERRA datasets. The Rossby waves are identified by a multivariate projection of the global horizontal winds and pseudo-geopotential-geopotential height on the eigensolutions of the linearized primitive equations on the sphere with a basic state at rest (the so-called normal-mode functions on the terrain-following

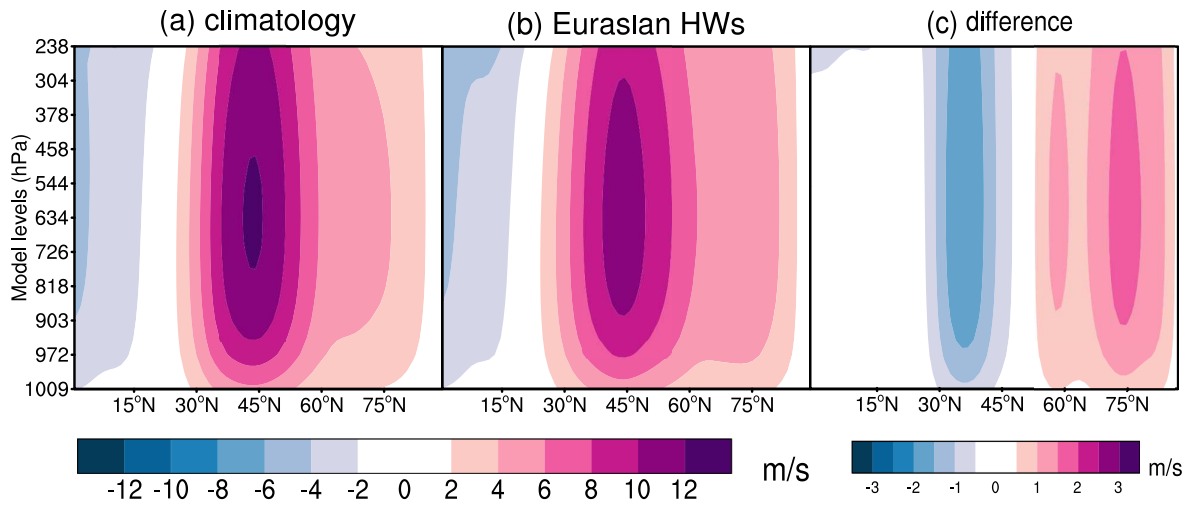


**Figure 9.** Zonal-mean zonal wind in the northern hemisphere troposphere in 1980-2019, May-Sep ERA5 data. (a) climatology, (b) Eurasian heat waves (HWs) and (c) climatology - heat waves.

485 levels functions). A complete projection basis provides global statistics of Rossby waves as a function of the zonal wavenumber, the meridional mode index and the vertical mode index - modes associated with the vertical structure functions spanning the troposphere and the stratosphere. Scale-selective Rossby wave filtering in physical space is seen as an advantage compared to univariate filtering using the Fourier series along the latitude circles. The reconstructed circulation that are barotropic within the troposphere.

490 The reconstructed physical space picture of the Eurasian heat waves is in agreement with previous studies (Lau and Kim, 2012; Behera et al. The enhancement of the zonal mean state ( $k = 0$ ) zonal winds in high latitude of the Northern Hemisphere is likely a component of more-persistent double jets over Eurasia during heat waves in Eurasia is dominated by recently discussed by Rousi et al. (2022). In modal space, this is seen as an increase of around 20% in the intramonthly variance in the zonal mean state asymmetrical Rossby mode with the meridional index 6 along with a similar decrease in the meridional mode 4. In physical  
 495 space, the anticyclonic circulation system over northeastern Europe with zonal wavenumbers 2 and 3, which is in agreement with previous studies dipole-shaped change of the zonal-mean zonal wind is such that the mean westerlies somewhat weaken near their core at 45°N but get twice stronger in high midlatitudes (centred at 75°N). A decreased barotropicity close to 45°N is interpreted as a reduced vertical shear of the mean westerly flow. Future work should couple these findings with the study by Wirth and Polster (2021) on the role of Rossby waves in processes leading to the double jet formation.

500 The statistical analysis is carried out on the complex time series of the Hough expansion coefficients representing Rossby modes with the barotropic tropospheric structures. The statistics is performed on the normalized energy anomalies for the total balanced (or Rossby-mode) circulation, for the zonal-mean state, and for planetary- and synoptic-scale waves. troposphere-barotropic structures. We show that the single-mode energies follow energy distribution of a single mode follows a  $\chi^2$ -distributions (as sums of squares of independent Gaussian real and imaginary parts). The energy distributions of the zonal-mean flow and

505 ~~the planetary distribution. Statistics of the normalized energy anomalies shows that the zonal mean state ( $k = 0$ ) and the planetary-scale ( $k = 1 - 3$ ) circulation are more skewed than other components the synoptic and smaller scales, with extended right tails. During the surface-~~

~~During the Eurasian heat waves, the skewness in planetary waves grows-increases while the opposite occurs in the zonal mean flow, confirming the mechanism of weakening zonal flow and amplification of planetary waves. The symmetric and asymmetric components of the circulation contribute equally to the changes during heat waves over Eurasia-~~

510 ~~Our main result is an increase in the skewness of the planetary wave energy anomalies during surface extremes. The increase in skewness can be linked with a decrease in the number of active degrees of freedom in state space during heat waves. A simple estimate This aligns with the results of Lucarini and Gritsun (2020) which are based on the atmospheric stability during Atlantic blockings. Based on the  $\chi^2$ -skewness shows, we estimate a reduction of the order of 1/4. This reduction yields a quantitative estimate for the well-known coarse structure of blocking events-~~

515 ~~We also discussed changes in time-averaged submonthly variance spectra in the zonal wavenumber domain. We find that the variance decreases for planetary scales and increases for synoptic scales, consistent with the prevalence of atmospheric blocking regime during surface heat waves. active degrees of freedom during Eurasian heat waves of about 25% compared to climatology.~~

520 ~~Our analysis of fingerprints of heat waves in the global balanced circulation can be applied to other extreme events as well as to the unbalanced component of the circulation~~ Consistent changes in wavenumber space are found in the intramonthly variance and entropy. Eurasian heat waves are characterised by a statistically significant increase of about 5% in the intramonthly variance at synoptic scales  $k = 7 - 8$ , with respect to climatology. This is consistent with increased synoptic activity during blocking (e.g., Shutts, 1983; Yamazaki and Itoh, 2013). In contrast, a reduction of intramonthly variance in  $k = 3$  of about 6%  
525 ~~is found not to be statistically significant. Future studies with longer datasets, such as climate model outputs are an opportunity for models' validation and larger datasets of extreme events.~~

530 *Code and data availability.* The ERA-Interim and ERA5 reanalysis datasets are available via <http://www.ecmwf.int>. The MERRA and JRA-55 are available at <https://gmao.gsfc.nasa.gov/reanalysis/MERRA> and <https://jra.kishou.go.jp/JRA-55>, respectively. The MODES software can be requested via <https://modes.cen.uni-hamburg.de>. The time series of the Hough expansion coefficients for the four reanalyses are available upon the request from the authors.

*Author contributions.* All authors contributed to the study conception and design. IS developed the algorithm, performed the data analysis and wrote a first draft of the manuscript. All authors participated in data interpretation and revised previous versions of the manuscript. All authors read and approved the final manuscript.

535 *Competing interests.* The authors declare that the research was conducted in the absence of any commercial or financial relationships that could be construed as a potential conflict of interest.

*Disclaimer.* TEXT

540 *Acknowledgements.* This work was funded by the Deutsche Forschungsgemeinschaft (DFG, German Research Foundation) under Germany's Excellence Strategy – EXC 2037 'CLICCS - Climate, Climatic Change, and Society' (CLICCS, A6) – Project Number: 390683824, contribution to the Center for Earth System Research and Sustainability (CEN) of ~~Universität Hamburg.~~ ~~IS thanks~~ Universität Hamburg. We thank the former MODES group members at the University of Ljubljana Damjan Jelić and Khalil Karami for the MODES decomposition of the four reanalysis data, to Žiga Zaplotnik for the advice on Python and his advice on processing the Hough coefficients in Python, to Qiyun Ma for the algorithm for the heat waves identification and discussion to Frank Sielmann for the variance analysis and technical support. We would also like to thank Valerio Lucarini for the discussion, and to two anonymous reviewers and Editor Dr. Gwendal Rivière for their constructive comments on the manuscript.

## 545 References

- Barriopedro, D., Fischer, E. M., Luterbacher, J., Trigo, R. M., and García-Herrera, R.: The Hot Summer of 2010: Redrawing the Temperature Record Map of Europe, *Science*, 332, 220–224, <https://doi.org/10.1126/science.1201224>, 2011.
- Behera, S. K., Ratnam, J. V., Masumoto, Y., and Yamagata, T.: Origin of extreme summers in Europe: the Indo-Pacific connection, *Clim. Dyn.*, 41, 663–676, <https://doi.org/10.1007/s00382-012-1524-8>, 2012.
- 550 Coumou, D., Petoukhov, V., Rahmstorf, S., Petri, S., and Schellnhuber, H. J.: Quasi-resonant circulation regimes and hemispheric synchronization of extreme weather in boreal summer, *Proc. Natl. Acad. Sci. U.S.A.*, 111, 12 331–12 336, <https://doi.org/10.1073/pnas.1412797111>, 2014.
- Coumou, D., Lehmann, J., and Beckmann, J.: Climate change. The weakening summer circulation in the Northern Hemisphere mid-latitudes, *Science (New York, N.Y.)*, 348, <https://doi.org/10.1126/science.1261768>, 2015.
- 555 Dee, D. P., Uppala, S. M., Simmons, A. J., Berrisford, P., Poli, P., Kobayashi, S., Andrae, U., Balmaseda, M. A., Balsamo, G., Bauer, P., Bechtold, P., Beljaars, A. C. M., van de Berg, L., Bidlot, J., Bormann, N., Delsol, C., Dragani, R., Fuentes, M., Geer, A. J., Haimberger, L., Healy, S. B., Hersbach, H., Hólm, E. V., Isaksen, I., Kållberg, P., Köhler, M., Matricardi, M., McNally, A. P., Monge-Sanz, B. M., Morcrette, J.-J., Park, B.-K., Peubey, C., de Rosnay, P., Tavolato, C., Thépaut, J.-N., and Vitart, F.: The ERA-Interim reanalysis: configuration and performance of the data assimilation system, *Q. J. R. Meteorol. Soc.*, 137, 553–597, <https://doi.org/10.1002/qj.828>, 2011.
- 560 Drouard, M. and Woollings, T.: Contrasting mechanisms of summer blocking over western Eurasia, *Geophys. Res. Lett.*, 45, 12–040, <https://doi.org/10.1029/2018GL079894>, 2018.
- Emerton, R., Brimicombe, C., Magnusson, L., Roberts, C., Di Napoli, C., Cloke, H. L., and Pappenberger, F.: Predicting the unprecedented: forecasting the June 2021 Pacific Northwest heatwave, *Weather*, n/a, <https://doi.org/https://doi.org/10.1002/wea.4257>, 2022.
- Feudale, L. and Shukla, J.: Influence of sea surface temperature on the European heat wave of 2003 summer. Part I: an observational study, *Clim. Dyn.*, 36, 1691–1703, <https://doi.org/10.1007/s00382-010-0788-0>, 2011.
- 565 Fuentes-Franco, R., Koenigk, T., Docquier, D., Graef, F., and Wyser, K.: Exploring the influence of the North Pacific Rossby wave sources on the variability of summer atmospheric circulation and precipitation over the Northern Hemisphere, *Clim. Dyn.*, pp. 1–15, <https://doi.org/10.1007/s00382-022-06194-4>, 2022.
- Galfi, V. M. and Lucarini, V.: Fingerprinting Heatwaves and Cold Spells and Assessing Their Response to Climate Change Using Large Deviation Theory, *Phys. Rev. Lett.*, 127, 058 701, <https://doi.org/10.1103/PhysRevLett.127.058701>, 2021.
- 570 Hersbach, H., Bell, B., Berrisford, P., Hirahara, S., Horányi, A., Muñoz-Sabater, J., Nicolas, J., Peubey, C., Radu, R., Schepers, D., et al.: The ERA5 global reanalysis, *Q. J. R. Meteorol. Soc.*, 146, 1999–2049, <https://doi.org/doi.org/10.1002/qj.3803>, 2020.
- Kasahara, A.: 3D Normal Mode Functions (NMFs) of a Global Baroclinic Atmospheric Model, *Modal View Of Atmospheric Variability: Applications Of Normal-Mode Function Decomposition in Weather and Climate Research*. N. Žagar and J. Tribbia, Eds., Springer, 575 *Mathematics of Planet Earth Series*, Vol.8, 2020.
- Kautz, L.-A., Martius, O., Pfahl, S., Pinto, J. G., Ramos, A. M., Sousa, P. M., and Woollings, T.: Atmospheric blocking and weather extremes over the Euro-Atlantic sector—a review, *Weather Clim. Dynam.*, 3, 305–336, <https://doi.org/10.5194/wcd-3-305-2022>, 2022.
- Kobayashi, S., Ota, Y., Harada, Y., Ebata, A., Moriya, M., Onoda, H., Onogi, K., Kamahori, H., Kobayashi, C., Endo, H., Miyaoka, K., and K., T.: The JRA-55 reanalysis: General specifications and basic characteristics, *J. Meteorol. Soc. Jpn. Ser. II*, 93, 5–48, 580 <https://doi.org/10.2151/jmsj.2015-001>, 2015.

- Kornhuber, K., Osprey, S., Coumou, D., Petri, S., Vladimir, P., and Stefan, R. and, G. L.: Extreme weather events in early summer 2018 connected by a recurrent hemispheric wave-7 pattern, *Environ. Res. Lett.*, 14, 054 002, <https://doi.org/10.1088/1748-9326/ab13bf>, 2019.
- Kornhuber, K., Coumou, D., Vogel, E., Lesk, C., Donges, J. F., Lehmann, J., and Horton, R. M.: Amplified Rossby waves enhance risk of concurrent heatwaves in major breadbasket regions, *Nat. Clim. Change*, 10, 48–53, <https://doi.org/10.1038/s41558-019-0637-z>, 2020.
- 585 Lau, W. K. and Kim, K.-M.: The 2010 Pakistan flood and Russian heat wave: Teleconnection of hydrometeorological extremes, *J Hydrometeorol.*, 13, 392–403, <https://doi.org/10.1175/JHM-D-11-016.1>, 2012.
- Lucarini, V. and Gritsun, A.: A new mathematical framework for atmospheric blocking events, *Clim. Dyn.*, 54, 575–598, <https://doi.org/10.1007/s00382-019-05018-2>, 2020.
- Ma, Q. and Franzke, C. L. E.: The role of transient eddies and diabatic heating in the maintenance of European heat waves: a nonlinear  
 590 quasi-stationary wave perspective, *Clim. Dyn.*, 56, 2983 – 3002, <https://doi.org/10.1007/s00382-021-05628-9>, 2021.
- Nakamura, N. and Huang, C. S.: Atmospheric blocking as a traffic jam in the jet stream, *Science*, 361, 42–47, <https://doi.org/10.1126/science.aat0721>, 2018.
- Park, M. and Lee, S.: Relationship between tropical and extratropical diabatic heating and their impact on stationary–transient wave interference, *J Atmos Sci*, 76, 2617–2633, <https://doi.org/10.1175/JAS-D-18-0371.1>, 2019.
- 595 Perron, M. and Sura, P.: Climatology of non-Gaussian atmospheric statistics, *J. Clim.*, 26, 1063–1083, <https://doi.org/10.1175/JCLI-D-11-00504.1>, 2013.
- Petoukhov, V., Rahmstorf, S., Petri, S., and Schellnhuber, H. J.: Quasiresonant amplification of planetary waves and recent Northern Hemisphere weather extremes, *Proc. Natl. Acad. Sci. U.S.A.*, 110, 5336–5341, <https://doi.org/10.1073/pnas.1222000110>, 2013.
- Ragone, F. and Bouchet, F.: Rare Event Algorithm Study of Extreme Warm Summers and Heatwaves Over Europe, *Geophys. Res. Lett.*s, 48,  
 600 <https://doi.org/10.1029/2020gl091197>, 2021.
- Rienecker, M. M., Suarez, M. J., Gelaro, R., Todling, R., Bacmeister, J., Liu, E., Bosilovich, M. G., Schubert, S. D., Takacs, L., Kim, G.-K., Bloom, S., Chen, J., Collins, D., Conaty, A., da Silva, A., Gu, W., Joiner, J., Koster, R. D., Lucchesi, R., Molod, A., Owens, T., Pawson, S., Pegion, P., Redder, C. R., Reichle, R., Robertson, F. R., Ruddick, A. G., Sienkiewicz, M., and Woollen, J.: MERRA: NASA’s Modern-Era Retrospective Analysis for Research and Applications, *Journal of Climate*, 24, 3624 – 3648, <https://doi.org/10.1175/JCLI-D-11-00015.1>,  
 605 2011.
- Rogers, C. D.: *Inverse Methods for Atmospheric Sounding: Theory and Practice*, Series on Atmospheric, Oceanic and Planetary Physics, World Scientific Publ., Singapore, 2000.
- Rousi, E., Kornhuber, K., Beobide-Arsuaga, G., Luo, F., and Coumou, D.: Accelerated western European heatwave trends linked to more-persistent double jets over Eurasia, *Nat Commun*, 13, 3851, <https://doi.org/https://doi.org/10.1038/s41467-022-31432-y>, 2022.
- 610 Schneidereit, A., Schubert, S., Vargin, P., Lunkeit, F., Zhu, X., Peters, D. H., and Fraedrich, K.: Large-scale flow and the long-lasting blocking high over Russia: Summer 2010, *Mon Weather Rev.*, 140, 2967–2981, <https://doi.org/10.1175/MWR-D-11-00249.1>, 2012.
- Screen, J. A. and Simmonds, I.: Amplified mid-latitude planetary waves favour particular regional weather extremes, *Nat. Clim. Change*, 4, 704–709, <https://doi.org/10.1038/nclimate2271>, 2014.
- Shutts, G.: The propagation of eddies in diffluent jetstreams: Eddy vorticity forcing of ‘blocking’ flow fields, *Q. J. R. Meteorol. Soc.*, 109,  
 615 737–761, <https://doi.org/10.1002/qj.49710946204>, 1983.
- Stefanon, M., D’Andrea, F., and Drobinski, P.: Heatwave classification over Europe and the Mediterranean region, *Environ. Res. Lett.*, 7, 014 023, <https://doi.org/10.1088/1748-9326/7/1/014023>, 2012.

- Sura, P., Newman, M., Penland, C., and Sardeshmukh, P.: Multiplicative noise and non-Gaussianity: A paradigm for atmospheric regimes?, *J. Atmos. Sci.*, 62, 1391–1409, <https://doi.org/10.1175/JAS3408.1>, 2005.
- 620 Teng, H. and Branstator, G.: A zonal wavenumber 3 pattern of Northern Hemisphere wintertime planetary wave variability at high latitudes, *J. Clim.*, 25, 6756–6769, <https://doi.org/10.1175/JCLI-D-11-00664.1>, 2012.
- Teng, H. and Branstator, G.: Amplification of Waveguide Teleconnections in the Boreal Summer, *Curr. Climate Change Rep.*, 5, 421 – 432, <https://doi.org/10.1007/s40641-019-00150-x>, 2019.
- Trenberth, K. E. and Fasullo, J. T.: Climate extremes and climate change: The Russian heat wave and other climate extremes of 2010, *J. Geophys. Res. Atmos.*, 117, <https://doi.org/10.1029/2012JD018020>, 2012.
- 625 Žagar, N., Kasahara, A., Terasaki, K., Tribbia, J., and Tanaka, H.: Normal-mode function representation of global 3D datasets: open-access software for the atmospheric research community, *Geosci. Model Dev.*, 8, 1169–1195, <https://doi.org/https://doi.org/10.5194/gmd-8-1169-2015>, 2015.
- Žagar N. and J., T.: Modal View of Atmospheric Variability: Applications of Normal-Mode Function Decomposition in Weather and Climate Research, *Mathematics of Planet Earth* 8, Springer International Publishing;Springer, 1st ed. edn., <https://doi.org/https://doi.org/10.1007/978-3-030-60963-4>, 2020.
- 630 Wiedenmann, J. M., Lupo, A. R., Mokhov, I. I., and Tikhonova, E. A.: The climatology of blocking anticyclones for the Northern and Southern Hemispheres: Block intensity as a diagnostic, *J. Clim.*, 15, 3459–3473, [https://doi.org/10.1175/1520-0442\(2002\)015<3459:TCOBAF>2.0.CO;2](https://doi.org/10.1175/1520-0442(2002)015<3459:TCOBAF>2.0.CO;2), 2002.
- 635 Wilks, D. S.: Statistical methods in the atmospheric sciences, vol. 100 of *International Geophysics*, Academic Press, third edn., <http://www.sciencedirect.com/science/bookseries/00746142/100/supp/C>, 2011.
- Wirth, V. and Polster, C.: The problem of diagnosing jet waveguidability in the presence of large-amplitude eddies, *J. Atmos. Sci.*, 78, 3137–3151, <https://doi.org/10.1175/JAS-D-20-0292.1>, 2021.
- Woollings, T., Barriopedro, D., Methven, J., Son, S.-W., Martius, O., Harvey, B., Sillmann, J., Lupo, A. R., and Seneviratne, S.: Blocking and its response to climate change, *Curr. Climate Change Rep.*, 4, 287–300, <https://doi.org/10.1007/s40641-018-0108-z>, 2018.
- 640 Xu, P., Wang, L., Liu, Y., Chen, W., and Huang, P.: The record-breaking heat wave of June 2019 in Central Europe, *Atmos. Sci. Lett.*, 21, e964, <https://doi.org/10.1002/asl.964>, 2020.
- Yamazaki, A. and Itoh, H.: Vortex–vortex interactions for the maintenance of blocking. Part I: The selective absorption mechanism and a case study, *J. Atmos. Sci.*, 70, 725–742, <https://doi.org/10.1175/JAS-D-11-0295.1>, 2013.
- 645 Žagar, N., Jelić, D., Blaauw, M., and Bechtold, P.: Energy spectra and inertia–gravity waves in global analyses, *J. Atmos. Sci.*, 74, 2447–2466, <https://doi.org/10.1175/JAS-D-16-0341.1>, 2017.
- Žagar, N., Kosovelj, K., Manzini, E., Horvat, M., and Castanheira, J.: An assessment of scale-dependent variability and bias in global prediction models, *Clim. Dyn.*, 54, 287–306, <https://doi.org/10.1007/s00382-019-05001-x>, 2019.
- Žagar, N., Zaplotnik, Ž., and Karami, K.: Atmospheric subseasonal variability and circulation regimes: spectra, trends, and uncertainties, *J. Clim.*, 33, 9375–9390, <https://doi.org/10.1175/JCLI-D-20-0225.1>, 2020.
- 650 Zhou, Y. and Wu, Z.: Possible impacts of mega-El Niño/Southern Oscillation and Atlantic Multidecadal Oscillation on Eurasian heatwave frequency variability, *Q. J. R. Meteorol. Soc.*, 142, 1647–1661, <https://doi.org/10.1002/qj.2759>, 2016.